Eur. Phys. J. Spec. Top. (2022) 231:4153–4165
https://doi.org/10.1140/epjs/s11734-022-00572-z

THE EUROPEAN
PHYSICAL JOURNAL
SPECIAL TOPICS

Review

Reliability and interpretation of the microstructural parameters determined by X-ray line profile analysis for nanostructured materials

Jenő Gubicza[a]

Department of Materials Physics, ELTE Eötvös Loránd University, POB 32, Budapest 1518, Hungary

Received 27 December 2021 / Accepted 9 April 2022 / Published online 27 April 2022
© The Author(s) 2022

Abstract In this overview, the applicability of X-ray diffraction line profile analysis (XLPA) for the characterization of the microstructure in nanostructured materials is overviewed. The dislocation densities obtained by whole pattern fitting and from the breadth of the diffraction peaks are compared. Both theoretical considerations and experimental evidences prove that the evaluation of the peak breadth solely is not suitable for the determination of the dislocation density. In addition, the microstructural parameters determined by XLPA were compared to the values obtained directly by microscopic methods. It was found that the ratio of the grain size obtained by microscopy and the crystallite size determined by XLPA decreases with the reduction of the grain size in nanomaterials, and below ~ 20 nm, the two values agree within the experimental error. In addition, correlation between the microstructural parameters (e.g., crystallite size and dislocation density) determined by XLPA was not found. It was revealed that bottom–up processing methods can produce similarly high defect density in nanostructured materials as severe plastic deformation (SPD). The influence of stacking fault energy, melting point, and degree of alloying on the microstructure of nanomaterials is discussed in detail.

1 Introduction

Nanostructured materials are in the forefront of materials science due to their unique properties, such as improved mechanical and magnetic performances [1,2]. The properties of nanomaterials can be tuned by changing the chemical composition and/or the microstructure, such as the size of grains, the character of grain boundaries, the amount, type and arrangement of dislocations, and planar faults [2,3]. The latter methodology can be called as "lattice defect engineering". The grain boundaries can also be considered as two-dimensional lattice defects; therefore, the well-known "grain boundary engineering" is a special type of this method [4,5]. "Lattice defect engineering" can be carried out by changing the processing conditions of nanomaterials or applying post-processing heat treatments [3,6]. This is valid for nanomaterials manufactured by either bottom–up or top–down processing techniques. In the case of top–down approach, the ultrafine-grained (UFG) or nanocrystalline materials are produced by severe plastic deformation (SPD) [1]. The imposed strain, the pressure, and temperature applied during SPD and the chemical composition of the material influence significantly the lattice defect structure in the as-processed samples [2,3]. On the other hand, for nanopowder sintering which is a bottom–up approach, the sintering conditions, such as pressure, temperature, and atmosphere, have a considerable effect on the grain size and the defects inside the grains [2].

For improving the performance of nanostructured materials by "lattice defect engineering", it is essential to possess experimental techniques for a reliable characterization of lattice defects. Microscopic methods, such as transmission electron microscopy (TEM), give direct observation of the microstructure as it is [7,8]. However, the studied volume is usually very small, resulting in an uncertainty whether the information deduced from the images characterize the whole sample. Alternatively, there are indirect methods which study much larger volumes, but in these cases, the features of the defect structure are extracted from the analysis of the recorded signals without seeing the real microstructure. Examples for these indirect techniques are electrical resistivity measurement, positron annihilation spectroscopy (PAS), and X-ray line profile analysis (XLPA) [9–18]. XLPA analyzes the diffraction peak shape on the basis of a model of the microstructure and yields the crystallite size distribution and the lattice defect structure with a good statistics and in a non-destructive way. Due to the indirect nature of XLPA, the reliability of the microstructural parameters determined by this technique is worth to check by comparing them with the results obtained by direct methods, such as TEM. In this paper, instructions are given for a proper application of XLPA on nanomaterials, and the microstruc-

[a] e-mail: jeno.gubicza@ttk.elte.hu (corresponding author)

tural parameters determined by this analysis and some other methods are compared. The efficiency of XLPA in the investigation of nanostructured materials is shown on illustrative examples.

2 Whole diffraction pattern fitting: a reliable method of XLPA

The broadening of the diffraction profiles is caused by the small size of crystallites (also called as diffraction domains), chemical heterogeneities [19], planar faults (e.g., twin boundaries, stacking faults or antiphase boundaries [20–22]), and lattice defects having long-range order strain field such as dislocations [18,23]. In addition, there is an instrumental broadening caused by the diffractometer. The intensity profiles resulted by these contributions are convoluted in the whole diffraction peak. Therefore, the profile shape depends on the following parameters of the microstructure: the median and the variance of the crystallite size distribution, a parameter describing the anisotropic shape of crystallites, the dislocation density, a parameter describing the arrangement of dislocations, the dislocation contrast factor depending on the prevailing slip systems of dislocations [23], and the probability of planar faults. Due to the numerous microstructural parameters influencing the intensity profiles, the most reliable evaluation of them can be achieved if the whole diffraction peak shape is evaluated and the procedure is performed not only for one peak but for all available reflections of the measured diffraction pattern. The evaluation of the entire profile is also desirable, because the microstructural parameters influence not only the peak breadth but also the whole shape of reflections. For instance, the increase of the variance of the crystallite size distribution results in a longer tail of the peaks [18]. Similar effect is observed if the dislocations are arranged into low-energy configurations such as dipoles or low-angle grain boundaries [18]. The usual way of this procedure is the fitting of the whole pattern by the sum of a background and the theoretical functions of the diffraction peaks. Each peak function is obtained as the convolution of the theoretical profiles of the different contributions (e.g., crystallite size, dislocations, and planar faults) and the instrumental profile. The theoretical peak profiles are usually calculated on the basis of a model of the microstructure. The theoretical profile formulas are collected in Ref. [18]. The calculated pattern function contains the unknown parameters of the microstructure and their values are determined by fitting the calculated pattern to the measured one. Numerous pattern fitting softwares are available freely in the Internet [24–26]; therefore, it is recommended to use one of them when an XRD pattern is needed to be evaluated for the microstructure of UFG or nanomaterials. As an example, Fig. 1 shows a whole diffraction pattern fitting on a nanocrystalline HfNbTiZr multi-principal element alloy (MPEA) processed by ten turns of high-pressure torsion (HPT) using the convolutional multiple whole profile (CMWP) fitting method [27]. It is noted that from the median and the variance of the crystallite size distribution, three different average mean crystallite sizes can be determined: the arithmetic mean as well as the area- and the volume-weighted mean crystallite sizes [18]. In this review, the area-weighted mean size is used for the characterization of the crystallite size. For instance, the CMWP fitting for HfNbTiZr MPEA processed by ten turns of HPT (shown in Fig. 1) resulted in 15 ± 2 nm for the area-weighted mean crystallite size and $(219 \pm 24) \times 10^{14}$ m^{-2} for the dislocation density.

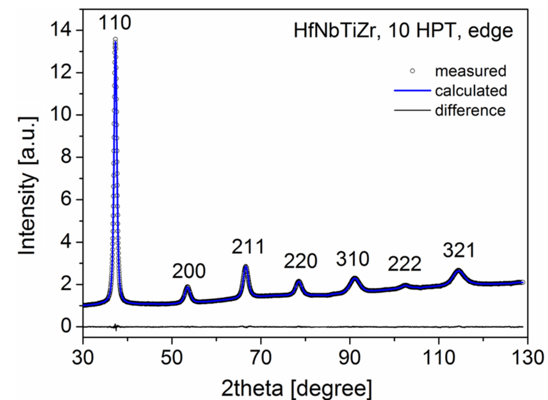

Fig. 1 Whole diffraction pattern fitting on a nanocrystalline HfNbTiZr MPEA processed by ten turns of HPT using the CMWP evaluation method

3 Dislocation density from the peak breadth: a wrong practice

There are studies in the literature which attempt to determine the dislocation density in nanomaterials only from the breadth of the diffraction profiles [28–30]. The most popular formula is the so-called Williamson–Smallman equation [31]

$$\rho = \frac{\sqrt{3}k\xi}{Db}, \tag{1}$$

where b is the magnitude of the Burgers vector of dislocations, ξ is the strain broadening over the magnitude of the diffraction vector, and D is the size of the blocks building up the microstructure. In the model of Williamson and Smallman, the dislocations are located on the interfaces between these blocks. In practice, D is taken as the size of the crystallites which is determined from the Williamson–Hall plot [32]. In this analysis, the full width at half maximum or the integral breadth of the XRD peaks is plotted as a function of the magnitude of the diffraction vector (see Fig. 2). The crystallite size (i.e., D) can be determined as the reciprocal of the intercept of the straight line fitted to the

datum points in the Williamson–Hall plot, while ξ is obtained as the slope of fitted straight line. Parameter k depends on the elastic moduli of the material and the arrangement of dislocations and its usual value is about 1.2 ± 0.2. There is another Williamson and Smallman formula which estimates the dislocation density only from the slope of the Williamson–Hall plot as [31]

$$\rho = \kappa \left(\frac{\xi}{b}\right)^2, \quad (2)$$

where the values of κ for face-centered cubic (fcc) and body-centered cubic (bcc) materials are 16.1 and 14.4, respectively.

It should be noted, however, that the two formulas presented above are not suitable for the determination of the dislocation density in general due to the following reasons:

1. Only the peak breadth is not enough for the determination of the dislocation density, since the width of reflection is influenced by both the density and the arrangement of dislocations. If dislocations form dipoles or low-angle grain boundaries, the peak breadth decreases even if the dislocation density remains unchanged. Therefore, the evaluation of the total intensity profile or its Fourier transform is needed for the determination of the dislocation density.
2. In Eq. (1), D is the size of the blocks formed by the arrangement of dislocations in the Williamson–Smallman model. There is no proof for the equivalence of D and the crystallite size determined from the Williamson–Hall plot.
3. Usually, both D and ξ are determined from the Williamson–Hall plot by fitting a straight line on the datum points. On the other hand, in many cases, the points in the Williamson–Hall plot do not follow a smooth curve, as illustrated in Fig. 2a where the peak breadth in the reciprocal space (full width at half maximum, FWHM with the unit of 1/nm) is plotted as a function of the magnitude of the diffraction vector g for the first six reflections of copper processed by 1 pass of equal-channel angular pressing (ECAP) at room temperature (RT). In this case, the dependence of the broadening on the indices of reflections *hkl* is caused by the anisotropic nature of the strain field of dislocations and the strong anisotropy of the elastic constants of copper. Thus, the straight lines fitted to the 111–222 and 200–400 reflection pairs differ, as shown in Fig. 2a, thereby resulting in different dislocation densities using the Williamson–Smallman method. In addition, the straight line fitted to 200–400 reflection pair resulted in a negative intercept yielding to a value of D less than zero which is a non-sense.
4. For elastically less anisotropic materials, the Williamson–Hall analysis can be performed easily, as shown in Fig. 2b. However, the following basic assumption of this method is not valid in general: the breadths of the peak profile contributions of the crystallite size, microstrain, and instrument are added linearly. This assumption is valid only, if all peak contributions are Lorentzian functions, but usually this is not the case.
5. Although the theoretical argumentation presented above has already proved that the peak breadth solely is not enough for the determination of the dislocation density, in this study, a comparison is made between the dislocation densities obtained by the Williamson–Smallman formulas [i.e., by Eqs. (1) and (2)] and sophisticated whole diffraction pattern fitting. This comparison is performed on different UFG and nanocrystalline materials processed by SPD and electrodeposition. The samples are listed in Table 1 together with the intercept and slope of the straight line fitted to the Williamson–Hall plot and the dislocation density values determined by Eqs. (1) and (2). The dislocation densities determined by the CMWP method are also listed in Table 1. Figure 3 shows a comparison between the dislocation densities determined by the CMWP method and from the peak breadth using Eq. (1). The difference between the dislocation density values is evident. Namely, for all samples, the dislocation density obtained from the peak breadth is significantly lower than the value determined by pattern fitting. One possible reason of this difference is that the apparent crystallite size, $D\backslash$, overestimates the block size of the dislocation structure in the Williamson–Smallman model systematically. In addition, Eq. (1) was calculated assuming a uniform distribution of dislocations, i.e., the shielding of the strain field of dislocations due to their clustering was disregarded. If the arrangement of dislocations into low-energy configurations was taken into account, the same microstrain would be related to a higher dislocation density. The dislocation density calculated from Eq. (2) also deviates considerably from the value determined by CMWP fitting (see Fig. 4). These experimental evidences also confirm the theoretical considerations listed above, i.e., the breadth methods are not suitable for the determination of the dislocation density. Rather, a full profile fitting is suggested.

4 Comparison of the microstructure parameters obtained by XLPA and other methods

It is very often observed that the crystallite size determined by XLPA is significantly smaller than the grain size obtained by microscopic methods, such as electron backscatter diffraction (EBSD) or TEM [48–51]. This difference can be explained by the fact that in EBSD and TEM, usually the volumes bounded by high-angle grain boundaries (HAGBs) with misorientations higher than 15° are taken as grains, while in XLPA, the mis-

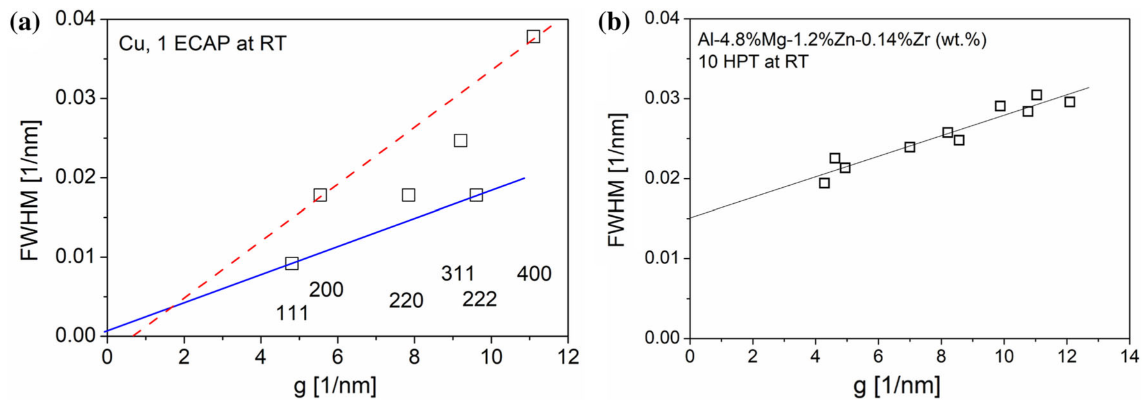

Fig. 2 Williamson–Hall plot for **a** a copper processed by one pass of ECAP at RT and **b** an Al alloy deformed by ten turns of HPT at RT. FWHM: full width at half maximum in the reciprocal space. g: magnitude of the diffraction vector. For the copper sample, the points do not follow a smooth trend due to the anisotropic strain broadening caused by dislocations. In this case, the blue solid and dashed red lines indicate fitting on 111–222 and 200–400 harmonic reflection pairs, respectively. For the Al alloy, all points were used in the fitting, since the elastic anisotropy of Al is low

Table 1 The slope and the intercept obtained by the Williamson–Hall (WH) analysis for the calculation of the dislocation density using Eqs. (1) and (2)

Sample	WH slope	WH intercept (1/nm)	Magnitude of Burgers vector (nm)	Dislocation density from Eq. (1) (10^{14} m^{-2})	Dislocation density from Eq. (2) (10^{14} m^{-2})	Dislocation density from CMWP [10^{14} m^{-2}]
Al-4.8%Mg-1.2%Zn-0.14%Zr, 10 HPT at RT	0.00128	0.0151	0.2872	1.3	3.0	8
Al-4.8%Mg-1.2%Zn-0.14%Zr, 4 ECAP at RT	0.002	0.0045	0.2872	0.6	7.3	4.8
Al-4.8%Mg-1.2%Zn-0.14%Zr, 8 ECAP at 473 K	0.0013	0.00183	0.2872	0.2	3.1	3.2
Al-5.7%Mg-1.9%Zn-0,35%Cu, 8 ECAP at 473K	0.0016	0.0026	0.2872	0.3	4.7	3.4
Ni-0.8%Al-0.3%Mo-0.3%Si-0.3%Fe, 5 HPT at RT	0.00489	0.01684	0.25	6.6	57	30
AM60, 10 HPT at RT	0.00724	1.67E−4	0.3203	0.08	77	11
Cu, 13 ECAR at RT	0.0029	0.0014	0.2564	0.3	19	21
HfNbTiZr, 20 HPT at RT	0.01532	0.02328	0.2974	24	398	214
316L, 10 HPT at RT	0.00757	0.02988	0.2482	18	140	133
Ni, ED	0.0075	0.0152	0.25	9.1	135	162
AZ80-SiC, 10 HPT at RT	0.00935	0.00006	0.3203	0.04	128	21
AM60, 2 ECAP at 493 K	0.00177	0.00694	0.3203	0.8	4.6	5.6
Cu-0.5%Zr, 1 RCB at 573 K	0.00168	0.00804	0.2564	1.1	6.4	45
Cu-0.5%Zr, 12 RCB at 573 K	0.0013	0.01083	0.2564	1.1	3.9	13
Ti, 10 RCB at RT	0.00266	0.00649	0.2951	1.2	12	6
Ni-1.9%Mo, ED	0.00323	0.00527	0.25	1.4	25	9
Ni-0.6%Mo, ED	0.002	0.0088	0.25	1.4	9.6	7.2
Ti, MF + rolling	0.00465	0.00693	0.2951	2.2	37	18

For comparison, the dislocation densities determined by the CMWP diffraction pattern fitting method are also listed. *HPT* high-pressure torsion, *ECAP* equal-channel angular pressing, *ECAR* equal-channel angular rolling, *ED* electrodeposition, *RCB* rotational constrained bending, and *MF* multidirectional forging. The processing conditions of the listed materials can be found in Refs. [27,33–47]

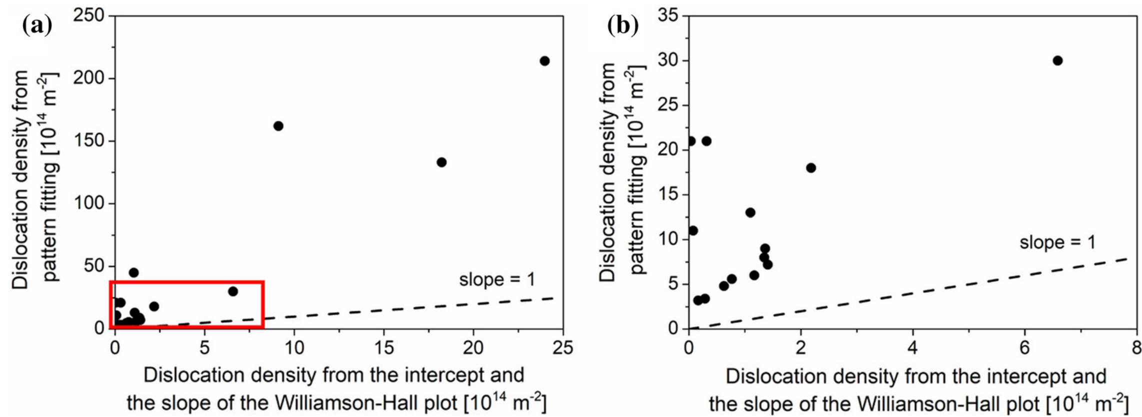

Fig. 3 **a** The dislocation density obtained by whole diffraction pattern fitting versus the same quantity calculated from the intercept and the slope of the Williamson–Hall plot using Eq. (1). Figure **b** shows the part of **a** corresponding to low dislocation densities (indicated by the red rectangle in **a**)

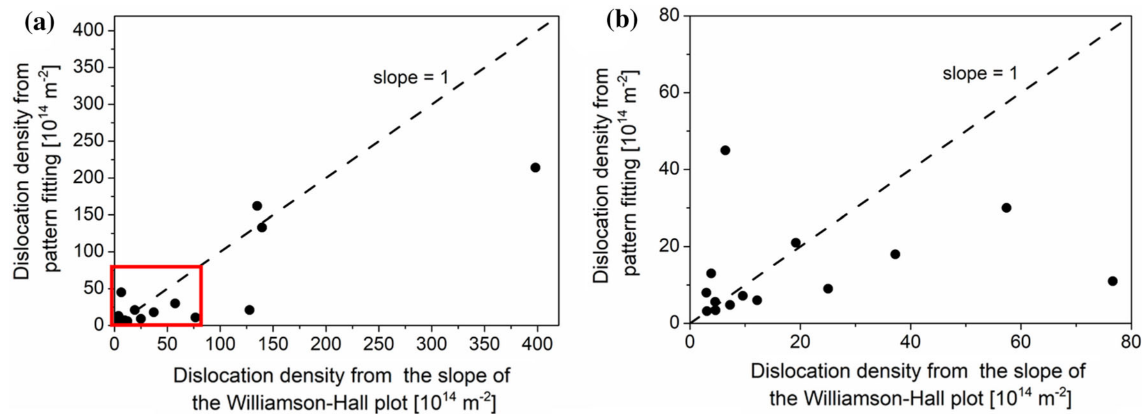

Fig. 4 **a** The dislocation density obtained by whole diffraction pattern fitting versus the same quantity calculated from the slope of the Williamson–Hall plot using Eq. (2). Figure **b** shows the part of **a** corresponding to low dislocation densities (indicated by the red rectangle in **a**)

orientation between the crystallites can be very small (it can be down to a few tenths of degree). Therefore, the crystallites correspond rather to subgrains and dislocation cells fragmenting the grains. Figure 5a shows the ratio of the grain and crystallite sizes determined by microscopic methods and XLPA, respectively, versus the grain size for fine grained materials processed by different techniques, including SPD, film deposition, and powder metallurgy. In Fig. 5b, a part of Fig. 5a corresponding to nanocrystalline materials is plotted with a higher magnification. The data in Fig. 5 were obtained on about 100 different samples. It is evident from this figure that there is no strict correlation between the grain and crystallite sizes determined by microscopic methods and XLPA, respectively. For instance, at the grain size of $\sim$ 400 nm, the ratio of the grain and crystallite size varied between 3 and 7. On the other hand, despite the scattering of the data, the samples with lower grain sizes usually have smaller crystallite sizes. In addition, Fig. 5b reveals that at the grain size of about 20 nm, the grain and crystallite sizes coincide (i.e., their ratio is $\sim$ 1), and below this limit, the two sizes do not show considerable difference. From this observation, we can conclude that below the grain size of $\sim$ 20 nm, the grains are not fragmented into subgrains or dislocation cells.

Figure 6a shows the dislocation density determined by XLPA versus the grain size obtained by microscopic methods for the same samples as used in Fig. 5. Due to the orders of magnitude difference between the dislocation density values, this quantity is plotted in logarithmic scale in Fig. 6. The general trend is that the finer microstructures contain more dislocations; however, strict correlation between the dislocation density and the grain size cannot be revealed. Indeed, for instance at the grain size of 200 nm, the dislocation density varies between $\sim$ 3 and $\sim$ 50 $\times 10^{14}$ m^{-2}. Figure 6b shows a part of Fig. 6a indicated by red rectangle with a higher magnification. The data plotted in Fig. 6b were obtained on nanocrystalline materials. The large scattering of the points in Fig. 6b indicates that there is no correlation between the dislocation density and the grain size for nanomaterials.

Figure 7 plots the crystallite size versus the dislocation density determined by XLPA for the samples investigated in the previous paragraphs. It seems that

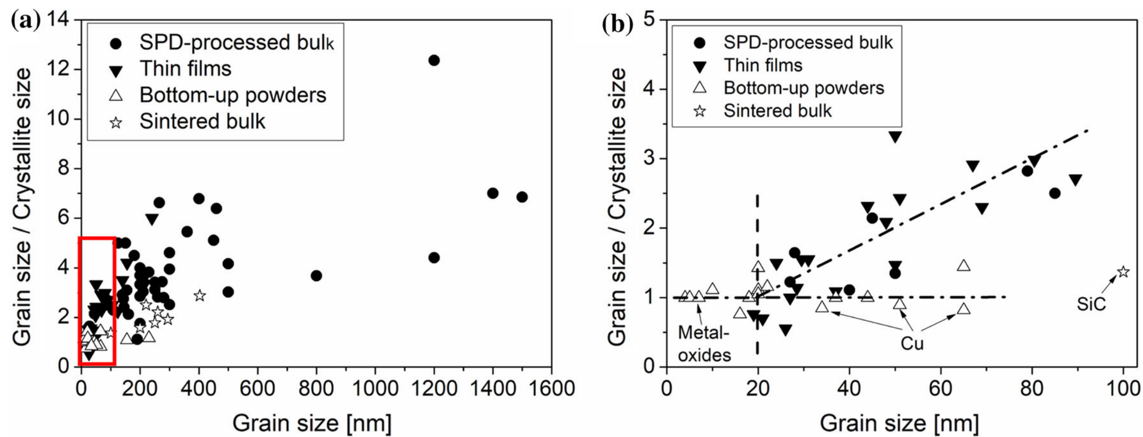

Fig. 5 **a** The ratio of the grain and crystallite sizes determined by microscopic methods (TEM or EBSD) and XLPA, respectively, versus the grain size. The part indicated by red rectangle in **a** and corresponds to nanocrystalline materials is magnified in Fig. **b**

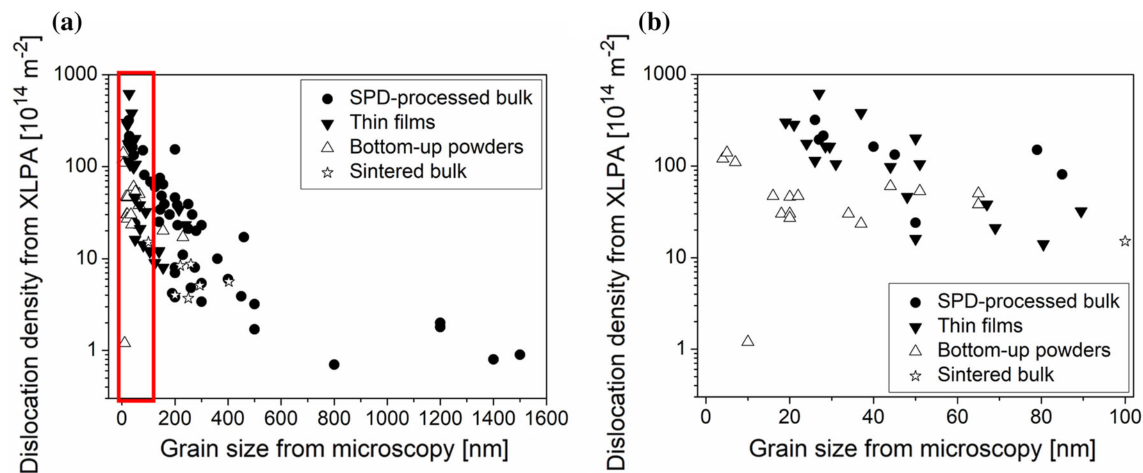

Fig. 6 **a** The dislocation density determined by XLPA versus the grain size determined by microscopic methods (TEM or EBSD). The part indicated by red rectangle in **a** and corresponds to nanocrystalline materials is magnified in Fig. **b**

the high dislocation densities were detected in the specimens having low crystallite sizes. On the other hand, strict correlation between the crystallite size and the dislocation density cannot be observed. For instance, for the crystallite size of about 20–30 nm, the dislocation density varies between ~ 10 and $\sim 600 \times 10^{14}\,\mathrm{m}^{-2}$ as indicated by the blue rectangle in Fig. 7. In addition, for the dislocation density of about 40–50 $\times 10^{14}\,\mathrm{m}^{-2}$, the crystallite size varies between 10 and 70 nm as indicated by the red rectangle in Fig. 7.

It is worth to compare the parameters of the microstructure determined by XLPA with the values determined by the other methods. Figure 8 shows the dislocation density obtained by XLPA versus the values determined by PAS for interstitial-free steel processed by different numbers of HPT turns at RT. The data were taken from Ref. [51]. A good agreement between the dislocation densities obtained by the two methods is revealed in Fig. 8.

The reliability of the twin fault probability determined by XLPA can be checked by TEM observation. The average twin boundary spacing can be determined from the TEM images and compared with the twin fault spacing (d_{twin}) calculated from the twin fault probability (β) obtained by XLPA using the following formula for fcc materials [18]:

$$d_{twin} = \frac{100 d_{111}}{\beta[\%]}, \quad (3)$$

where d_{111} is the interplanar spacing for planes {111}, since twin boundaries exist on these planes in fcc crystals. Figure 9 compares the twin fault spacing values obtained by the direct method TEM and the indirect method XLPA for different UFG and nanocrystalline fcc materials: SPD-processed Cu [52], Ag [53] and equimolar CoCrFeNiMn alloy [54], electrodeposited Ni and Ni–Mo films [55], and sintered SiC [56]. The relatively good agreement between the twin fault spacing values obtained by TEM and XLPA confirms the reliability of the twin fault probability determined by the latter analysis. It should be noted, however, that XLPA usually investigates a much larger (about eight orders of magnitude higher) volume than TEM [18]; therefore,

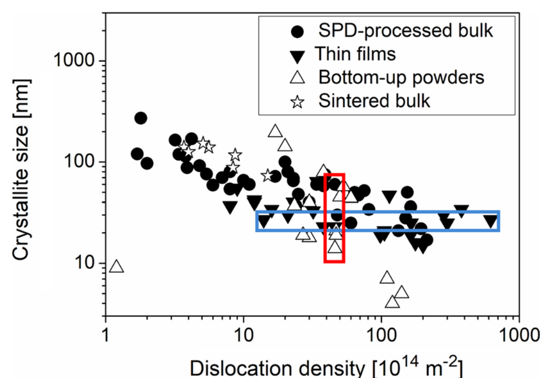

Fig. 7 The crystallite size versus the dislocation density. Both quantities were obtained by XLPA for different materials. The red and blue rectangles indicate the scattering of the crystallite size and the dislocation density, respectively, for a selected value of the dislocation density and the crystallite size

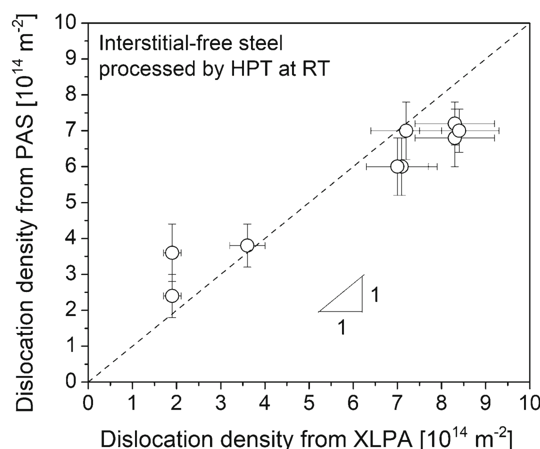

Fig. 8 The correlation between the dislocation density values obtained by XLPA and PAS for interstitial-free steel processed by different numbers of HPT turns at RT

some differences between the values obtained by the two methods are acceptable. In general, the statistics of the microstructure parameters determined by XLPA is significantly better and that for the values obtained by TEM.

In the previous sections, it was confirmed that XLPA is a reliable method for the characterization of the microstructure if the evaluation is performed by full pattern fitting. In the next section, this methodology is used for revealing the correlation between the processing methods and lattice defect structure in nanostructured materials.

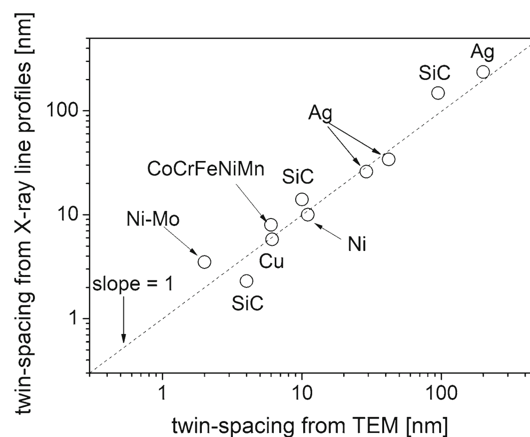

Fig. 9 The correlation between the mean twin-spacing determined by XLPA and TEM for different UFG and nanocrystalline fcc materials

5 Influence of processing methodology on lattice defects in nanomaterials

5.1 Effect of properties of materials on defect density developed during SPD processing

SPD processing of metals and alloys results in grain refinement and an additional increase of the density of dislocations and other lattice defects such as vacancies and planar faults [2]. With increasing the strain imposed during SPD, the dislocation density tends to saturate [48]. The maximum dislocation density is achieved as a result of the dynamic equilibrium between the multiplication and annihilation of dislocations during SPD. The basic mechanism of edge dislocation annihilation is climb which is controlled by vacancy diffusion [57]. Therefore, the saturation dislocation density depends on the rate of vacancy diffusion. The activation energy of vacancy diffusion is given as the sum of the energies of formation and migration of vacancies. Since, in SPD-processed materials, very high vacancy concentration (in the order of magnitude of 10^{-4} which is about 17 orders of magnitude greater than the equilibrium value) forms at the imposed strains corresponding to the saturation state [10,58–62], therefore many vacancies are available, i.e., only their motion must be activated. The vacancy migration activation energy, E_{VM}, is a monotonous function of the melting point, T_{M}, for pure fcc metals, as shown for Al, Ni, Cu, Au, and Ag in Table 2. Therefore, the lower the melting point, the easier the vacancy migration, thus the lower the maximum dislocation density. Indeed, Table 2 reveals that the saturation dislocation density is the smallest for Al having a relatively low melting point among the fcc metals. It should be noted, however, that Ag has a much higher dislocation density than Ni despite the 40% lower melting point as compared to Ni. The high saturation dislocation density in silver was caused by the large degree of dislocation dissociation in the former material [53]. The high equilibrium

splitting distance between partial dislocations in Ag is caused by the low SFE. Indeed, Table 2 shows that the splitting distance between partials, d_{p}, for Ag is 6.4 nm for edge dislocations which is much higher than for the other studied fcc metals which significantly hinders the climb of edge dislocations [53]. Although the splitting distance for screw dislocations is lower than for edge dislocations, it is also very high for silver (about 2.5 nm) in comparison with other fcc metals (lower than 1 nm). In the case of screw dislocations, the high splitting distance impedes cross-slip, i.e., also contributes to a less active dislocation annihilation in Ag. The splitting distance between partials depends not only on the SFE but also on the shear modulus as [57]

$$d_p = A\frac{Gb^2}{\gamma}, \tag{4}$$

where γ is the SFE, G is the shear modulus, b is the magnitude of the Burgers vector, and A is a constant having values of 0.019 and 0.048 for screw and edge dislocations, respectively [57]. Cu and Au have similar melting points and splitting distance values; thus, their saturation dislocation densities are also similar. It is worth noting that despite the much higher melting point of Ni compared to Cu or Au, the saturation dislocation density is not higher than for the latter two metals. Most probably, the lower splitting distance between partials for Ni facilitates dislocation annihilation which compensates the opposite effect of the higher melting point, resulting in similar maximum dislocation density values for Ni and Cu (or Au).

Beside the properties of the material, the SPD conditions, such as strain rate and pressure, may also influence the defect structure in the as-processed samples. For instance, the high applied pressure in HPT processing may yield an elevated saturation dislocation density compared to other SPD methods, such as ECAP [50,52], since the hydrostatic component of the stress field hinders the motion of vacancies by increasing the activation enthalpy. This effect is visible in the much higher saturation dislocation density in HPT-processed Cu (37×10^{14} m^{-2}) as compared to the counterpart deformed by ECAP at RT (21×10^{14} m^{-2}) [52]. The difference between the dislocation densities achieved by HPT and ECAP is more pronounced for silver (see Table 2) [50]. On the other hand, the maximum dislocation density values achieved by ECAP and HPT are similar for Al and Ni. In the latter cases, the splitting distance between partials is relatively small compared to Cu and Ag; therefore, when the high pressure is released after HPT processing, a portion of the dislocation density can be annihilated due to the very high excess vacancy concentration which facilitates diffusion. For Cu and Ag, the high splitting distance between partials impedes dislocation annihilation effectively after HPT processing; therefore, the difference between the dislocation densities obtained by ECAP and HPT remains detectable ex-situ. The decrease of the dislocation density after releasing the pressure applied in HPT processing has been shown by in-situ X-ray synchrotron experiments [64].

The lower SFE is associated with a lower twin boundary (or twin fault) energy; therefore, SPD processing yields a considerable value of twin fault probability in fcc metals having low SFE [50,54]. XLPA has revealed that similar to other defects the twin fault probability value increased with increasing the imposed strain during SPD, and then saturated [50,54]. For Au and Ag processed by ECAP at RT, the saturation twin fault probability values were 0.3 and 1.5%, respectively [53,65]. HPT at RT resulted in a higher twin fault probability in Ag (2.1%) as compared to ECAP processing [50]. During HPT of silver, the higher dislocation density compared to ECAP can yield a higher probability of the formation of Lomer–Cottrell locks which are preferred locations of mechanical twinning. Therefore, a higher twin fault probability can be measured after HPT as compared to ECAP.

Solute alloying or impurity elements have a pinning effect on dislocations, thereby hindering their annihilation during SPD processing. Therefore, with increasing the solute concentration, the saturation dislocation density is enhanced. For instance, 1 at.% of Mg in Al increased the maximum achievable dislocation density from 1.8 to 3.9×10^{14} m^{-2} during ECAP processing [48]. If the Mg concentration increased to 3%, the dislocation density further increased to $\sim 23 \times 10^{14}$ m^{-2} after ECAP processing at RT [48]. Similar effect can be detected if the alloying elements formed precipitates.

Table 2 The saturation dislocation density achieved by ECAP and HPT at RT in pure fcc metals

Material	Saturation dislocation density for ECAP/HPT (10^{14} m^{-2})	T_{m} (K)	E_{VM} (kJ/mol)	G (GPa)	γ (mJ/m^2)	d_{p} (nm)
Al	1.8/1.4	933	60	26	166	0.6
Ni	18/25	1728	120	82	125	2.0
Cu	21/37	1358	81	47	45	3.3
Au	17/n.a.	1337	80	27	32	3.4
Ag	46/154	1235	64	30	19	6.4

The material parameters influencing the maximum dislocation density are also listed. T_m melting point, E_{VM} vacancy migration energy, G shear modulus, γ stacking fault energy, d_p splitting distance between partials in dissociated edge dislocations. The experimental E_{VM} values were taken from Ref. [63]

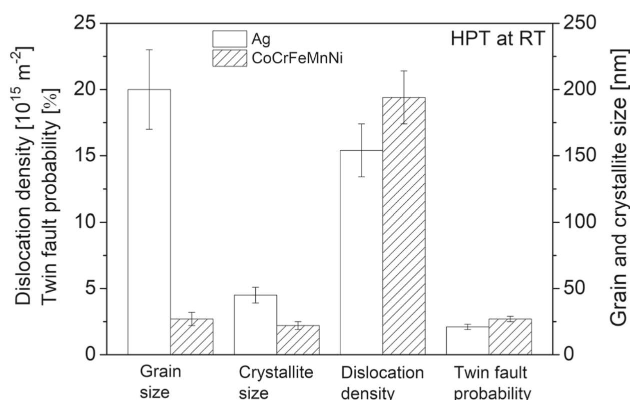

Fig. 10 Comparison of the parameters of the microstructure for 4N purity silver and CoCrFeMnNi HEA processed by HPT until microstructure saturation. For both materials, the SFE is about 19–22 mJ/m^2

For instance, in ECAP-processed Al–4.8%Zn–1.2%Mg–0.14%Zr (wt%) alloy with η-$MgZn_2$ precipitates the dislocation density saturated at the value of $\sim 5 \times 10^{14}$ m^{-2} which is much larger than that for pure Al ($\sim 1.8 \times 10^{14}$ m^{-2}) [41]. The increase of the dislocation density due to alloying is usually accompanied by the refinement of the grain size [2].

The alloying effect on the defect density and the grain size can be increased by increasing the alloying element content. With gradually enhancing the concentration of alloying atoms, we can achieve a state when the solute and solvent element contents are equal. These materials are called as multi-principal element alloys (MPEAs) or complex concentrated alloys (CCAs) [66,67]. The most frequently studied CCA is the so-called Cantor alloy with the equimolar composition of CoCrFeMnNi [67]. This material has similarly low SFE (22 mJ/m^2) as for pure silver (19 mJ/m^2); therefore, the defect densities in the two materials processed under the same SPD conditions are worth to compare. Figure 10 shows the grain size, crystallite size, dislocation density, and twin fault probability for CoCrFeMnNi alloy and pure Ag processed by HPT at RT [50,54]. It seems that CoCrFeMnNi alloy has a one order of magnitude smaller grain size and a slightly higher density of lattice defects (dislocations and twin faults). This difference can be explained by the more retarded defect annihilation caused by the 26% higher melting point (1562 K for CoCrFeMnNi versus 1235 K for Ag) and the 2.7 times higher shear modulus (80 GPa versus 30 GPa for Ag), since the latter difference caused a much larger splitting distance between partials (11.3 nm for CoCrFeMnNi versus 6.4 nm for Ag in the case of edge dislocations). The higher degree of dislocation dissociation for CoCrFeMnNi could cause the higher twin fault probability (2.7% versus 2.1% for Ag), since the dissociation into distant partials is a basic mechanism of deformation twinning in fcc materials [2].

In general, alloying is of great importance in the achievement of high defect density and small grain size in SPD-processed materials. Thus, the highest saturation dislocation density and the smallest minimum grain size values can be obtained in highly alloyed materials, as it is demonstrated in Fig. 11a. In that figure, the saturation grain size versus the corresponding maximum achievable dislocation density is plotted for different SPD-processed metals and alloys. It is evident that SPD was the most effective for CoCrFeNi, CoCrFeMnNi, and Cu-27%Cr alloys among the investigated materials [54,68,69]. The very small grain size and the high defect density in SPD-processed alloys yield an outstanding saturation yield strength, as shown in Fig. 11b, where the saturation yield strength versus the maximum dislocation density is plotted for some SPD-processed fcc alloys. The highest yield strength was obtained for CoCrFeNi and CoCrFeMnNi MPEAs with the value of about 1700 MPa [69].

5.2 Comparison of the defect densities developed in nanomaterials processed by top–down and bottom–up approaches

It is evident that the SPD-processed nanostructured materials should contain a high density of lattice defects, since during plastic deformation at high strains many defects, such as vacancies, dislocations and grain boundaries form [2]. On the other hand, it is not clear whether the nanomaterials produced by bottom–up approaches have lower, similar or higher defect density than in the SPD-processed counterparts. Therefore, systematic studies were conducted for the comparison of defect densities in nanostructured materials having the same or very similar compositions but processed by essentially different methods [55]. As an example, Fig. 12 shows the dislocation density for pure Ni, Ni–0.5% Mo and Ni–5% Mo alloys (at%) produced by the top–down method of HPT and the bottom–up technique of electrodeposition (ED) [55,70]. It can be seen that the dislocation density in the ED-processed samples is similarly high than that for the counterparts deformed by HPT. Even more, the dislocation density for the electrodeposited Ni–5% Mo alloy is about twice than that obtained on the same composition processed by HPT [55]. The grain sizes for pure Ni and the low-alloyed Ni were similar (about 200 nm) for both the HPT-processed and the electrodeposited materials [55]. On the other hand, for highly alloyed Ni–5% Mo, electrodeposition yielded a much smaller grain size ($\sim$ 26 nm) than that in the sample processed by HPT at RT ($\sim$ 125 nm). This difference is in line with the higher dislocation density in the electrodeposited Ni–5% Mo alloy (see Fig. 12).

Although bottom–up methods can produce similar high lattice defect density as SPD processing, their evolution history is different. Namely, during SPD, the external stresses induce dislocation multiplication, resulting in an increase of the dislocation density which saturates when this multiplication and the annihilation of dislocations get in dynamic equilibrium. The mechanisms of dislocation annihilation are strongly influenced

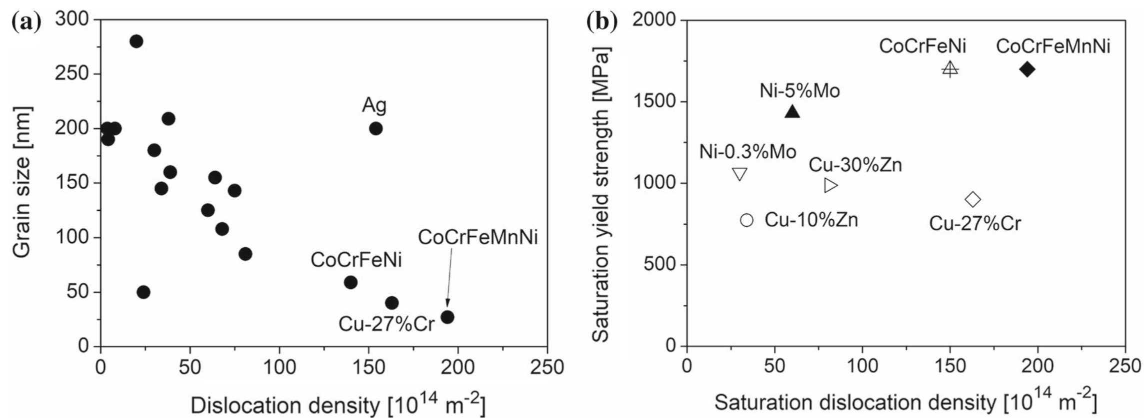

Fig. 11 The grain size versus the dislocation density for different metals and alloys processed by SPD until saturation. The samples possessing the highest saturation dislocation densities are indicated by their compositions. **b** The saturation yield strength versus the saturation dislocation density for different SPD-processed fcc alloys

by the material properties (e.g., the melting point, the shear modulus, and the stacking fault energy) as shown in Sect. 5.1; therefore, the saturation dislocation density depends mainly on these properties. On the other hand, in nanomaterials processed by bottom–up methods, the lattice defects form during growing of the nanosized grains. These grown-in defects often form in order to reduce the mismatch stresses between the grains at the non-coherent grain boundaries. Therefore, the density of the grown-in defects is rather determined by the processing parameters controlling the grain size (e.g., the current density, pH, organic additive content in the electrolyte bath, etc.) than the properties of the base material. As a result, the dislocation density can be much higher in the materials manufactured by bottom–up methods than in the SPD-processed counterparts having similar compositions (as an example, see Ni–5% Mo alloy in Fig. 12). Moreover, stacking and twin faults can form in high SFE materials processed by bottom–up techniques which does not occur during SPD. For instance, the Ni–5% Mo alloy obtained by electrodeposition has a twin fault probability of $\sim 3.9\%$ which was not observed in the same alloy deformed by HPT due to the high SFE of this Ni alloy. Twin faults (or twin boundaries) also contribute to the accommodation of misorientations in the as-deposited layers; thus, their formation is reasonable even if the SFE is not low. Comparable small grain sizes and high defect densities were developed also in MPEAs processed by bottom–up and top–down techniques [70]. As an illustration, Fig. 13 compares the microstructure parameters in equimolar CoCrFeNi MPEA samples manufactured by 20 turns of HPT at RT and physical vapor deposition (PVD) technique [70]. PVD resulted in smaller grain and crystallite sizes as well as a higher dislocation density than HPT processing. As the SFE is low for CoCrFeNi alloy (~ 22 mJ/m^2), significant twin fault probability was detected not only in the PVD film ($\sim 1.6\%$) but also in the bulk specimen processed by HPT ($\sim 2.6\%$). It should be noted that in Co–Cr–Fe–Ni PVD film with non-equimolar composition the twin fault probability can be increased even up to $\sim 4.6\%$ [70].

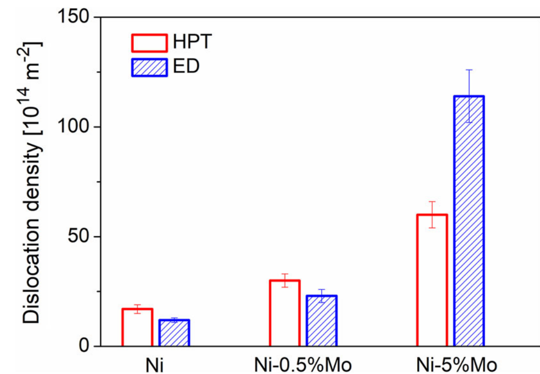

Fig. 12 Comparison of the maximum dislocation densities obtained on pure Ni and Ni–Mo alloys processed by SPD using HPT technique and electrodeposition (ED)

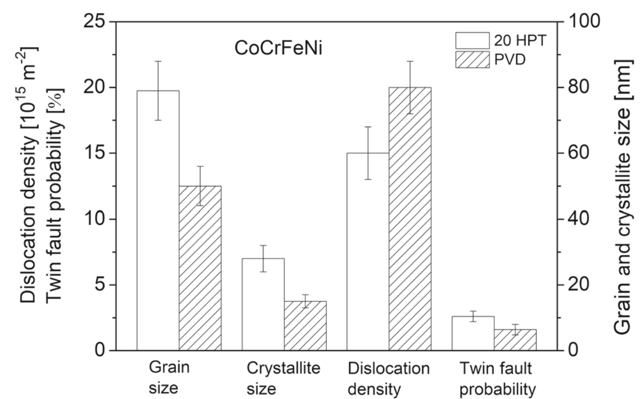

Fig. 13 Comparison of the parameters of the microstructure for nanocrystalline equimolar CoCrFeNi MPEA processed by HPT until microstructure saturation and physical vapor deposition (PVD)

It is worth noting that extremely high dislocation density ($\sim 600 \times 10^{14}$ m^{-2}) and large twin fault proba-

bility ($\sim 3.6\%$) can be detected in electroplated Ni even without alloying elements [71]. Namely, the addition of organic additives, such as saccharin or cysteine, to the electrolyte bath can reduce the grain size to about 20 nm which was accompanied by the development of a high dislocation density and twin fault probability during electrodeposition [71,72]. The very small grain size and the large defect density yielded an extremely high hardness of about 7 GPa in Ni. It is noticed that short post-processing heat treatment at moderate temperatures (at the homologous temperature of about 0.35) can result in an additional increase in hardness without reducing the ductility for nanomaterials processed by either SPD or bottom–up techniques [6]. For instance, in Ni deposited from a bath containing 0.4 g/L cysteine warming up to 500 K yielded an increase of the hardness from ~ 7 to ~ 8.4 GPa [71]. For highly alloyed nanomaterials, the optimum annealing temperature and the maximum hardening due to heat treatment increase. For electrodeposited Ni–18.7%Mo alloy film, annealing at 800 K for 1 h yielded a hardness enhancement from $\sim$ 6 GPa to $\sim$ 11 GPa [73,74]. This phenomenon is called as anneal-hardening and caused by the annihilation of mobile dislocations and the clustering of the remaining dislocations in SPD-processed materials. The latter effect was revealed by XLPA [75]. In addition, the relaxation of grain boundaries into a more equilibrium state and the segregation of solute atoms to grain boundaries in alloys retard the emission of mobile dislocations from boundaries and impede grain boundary sliding mechanism, thereby contributing to hardening [6].

It should be noted that XLPA is also suitable for the characterization of anisotropic nanostructures formed either by bottom–up or top–down methods. For crystallites with elongated shape, both the size distribution and the aspect ratio can be determined from the analysis of the diffraction pattern. For instance, carbon black nanocrystals processed by a bottom–up technique and having anisotropic shape were modelled by ellipsoids of revolution where the axis of revolution was taken perpendicular to the basal plane of the hexagonal crystal lattice [76]. Based on this model, the diffraction profile was calculated for the different reflections and fitted to the measured pattern, yielding the size and the ellipticity of the crystallites. The latter parameter describes the shape of crystallites: for spherical particles, the ellipticity is one while for flat crystallites its value is lower than one. The analysis revealed that thermal decomposition of hydrocarbon gases yielded flat carbon black crystals with an ellipticity of about 0.5 and an average size of ~ 4 nm. Heat treatment at 2700 °C for 20 min resulted in a fourfold coarsening and spheroidization of the crystallites [76]. For ZnO nanocrystals with a shape of hexagonal prism, XLPA determined the width and the height of the crystallites as ~ 9 and ~ 21 nm, respectively [77]. These nanoparticles were processed by a bottom–up method, namely, thermal decomposition of a $Zn(OH)_4(NO3)_2$ precursor. It is noticed that although elongated grains also often form in metals processed by top–down SPD techniques, the XRD patterns of these materials can be evaluated by the model of spherical crystallites, since the subgrains corresponding to the crystallites usually have isotropic shape [2]. In nanocrystalline thin films processed by bottom–up approaches (e.g., electroplating or sputtering), very often, the lattice defects such as dislocations and planar faults have a preferred orientation relative to the direction of the layer growth. This type of anisotropy can also be handled in XLPA evaluation. For instance, in a magnetron sputtered Cu foil, the twin boundaries were aligned strictly parallel to the surface of the film; therefore, the XLPA procedure developed for isotropic defect distribution had to be modified [22]. The improved CMWP fitting method revealed a relatively low dislocation density ($\sim 4 \times 10^{14}$ m^{-2}) and a high twin fault probability of about 3.8 %. Additional rolling of the sputtered Cu film yielded an increase of the dislocation density to $\sim 27 \times 10^{14}$ m^{-2}, while the twin fault probability was reduced to 3%. The dislocation structure in nanocrystalline films may also be anisotropic. For instance, in Cu–Nb multilayers having layer thicknesses of a few tens of nanometers, the Burgers vectors of grown-in dislocations were parallel to the foil plane in both layers [78]. In the Cu layers, the glide planes of these dislocations were parallel to the film plane, while in the Nb layers, they were inclined to the foil plane. Even if the dislocation orientation was anisotropic, XLPA was able to reveal that both Cu and Nb layers had a very high dislocation density (in the order of magnitude 10^{16} m^{-2}).

6 Summary

This overview demonstrates the efficiency of XLPA method on the study of microstructure in nanomaterials. Suggestions were made for achieving the highest reliability of this method, and the experimentally determined parameters of the microstructure were compared with the results of other methods. The influence of the properties of materials and the processing conditions on the microstructure were revealed with the help of XLPA technique. The results are summarized in the next paragraphs.

1. The evaluation of the diffraction peak breadth only is not suitable for the determination of the dislocation density. Rather, a full pattern fitting is necessary. The dislocation density and the twin fault probability determined by XLPA were in a reasonable agreement with the values obtained by other methods, such as TEM or PAS.
2. Although, materials with lower grain size usually contain a higher density of lattice defects (e.g., dislocations), there is no strict correlation between these parameters of the microstructure. The ratio of the grain and crystallite sizes determined by TEM and XLPA, respectively, is usually smaller for finer microstructures, and at the grain size of about 20 nm, this ratio becomes ~ 1, i.e., there is no considerable difference between the grain and crystallite

sizes. This result indicates that below this critical grain size, the grains are not fragmented into subgrains or dislocation cells.
3. For UFG and nanocrystalline pure metals processed by SPD at RT, the saturation dislocation density is determined by the melting point, the shear modulus, and the SFE. Alloying either in the form of solute atoms or precipitates refines the microstructure and increases the saturation dislocation density. The highest defect density and the smallest grain size were achieved in highly alloyed materials such as MPEAs including HEAs.
4. The defect density can be similar or even higher in nanomaterials processed by bottom–up methods in comparison with the samples having similar chemical composition but processed by SPD. The grain size is also similar or finer in the nanomaterials obtained by bottom–up approaches. In these specimens, dislocations, grain boundaries, stacking, and twin faults are grown-in defects which reduce the mismatch stresses between the grains in the as-processed materials. Thus, in the samples manufactured by bottom–up methods, the defect density is determined rather by the processing conditions and not the properties of the basic material. As a result, considerable twin fault probability can be observed even in materials with high SFE.
5. Short post-processing annealing at moderate temperatures can yield the improvement of the mechanical performance of nanomaterials due to the relaxation of the defect structure. Therefore, this anneal-hardening is suggested to apply in crystal defect engineering of nanomaterials. It was also demonstrated that XLPA is able to determine the parameters of the microstructure even if the shape of crystallites and/or the arrangement of lattice defects are anisotropic in nanostructured materials.

Acknowledgements The author is grateful to his former co-workers for their help in studying different ultrafine-grained and nanocrystalline materials.

Funding Information Open access funding provided by Eötvös Loránd University.

Open Access This article is licensed under a Creative Commons Attribution 4.0 International License, which permits use, sharing, adaptation, distribution and reproduction in any medium or format, as long as you give appropriate credit to the original author(s) and the source, provide a link to the Creative Commons licence, and indicate if changes were made. The images or other third party material in this article are included in the article's Creative Commons licence, unless indicated otherwise in a credit line to the material. If material is not included in the article's Creative Commons licence and your intended use is not permitted by statutory regulation or exceeds the permitted use, you will need to obtain permission directly from the copyright holder. To view a copy of this licence, visit http://creativecommons.org/licenses/by/4.0/.

References

1. R.Z. Valiev, A.P. Zhilyaev, T.G. Langdon, *Bulk Nanostructured Materials, Fundamentals and Applications* (Wiley, Hoboken, 2014)
2. J. Gubicza, *Defect Structure and Properties of Nanomaterials* (Woodhead Publishing, Duxford, 2017)
3. J. Gubicza, Mater. Trans. **60**, 1230 (2019)
4. T. Fujita, Z. Horita, T.G. Langdon, Mater. Sci. Eng. A **371**, 241 (2004)
5. M. Kumar, A.J. Schwartz, W.E. King, Acta Mater. **50**, 2599 (2002)
6. J. Gubicza, Adv. Eng. Mater. **22**, 1900507 (2020)
7. P. Buseck, J. Cowley, L. Eyring, *High-Resolution Transmission Electron Microscopy and Associated Techniques* (Oxford University Press, New York, 1988)
8. D.B. Williams, C. Barry Carter, *Transmission Electron Microscopy a Textbook for Materials Science* (Springer, New York, 2009)
9. R.M.J. Cotterill, Philos. Mag. **6**, 1351 (1961)
10. D. Setman, E. Schafler, E. Korznikova, M.J. Zehetbauer, Mater. Sci. Eng. A **493**, 116 (2008)
11. I. Prochazka, Mater. Struct. **8**, 55 (2001)
12. P. Hautojarvi, *Positrons in Solids* (Springer, Berlin, 1979)
13. J. Cizek, I. Prochazka, M. Cieslar, R. Kuzel, J. Kuriplach, F. Chmelik, I. Stulikova, F. Becvar, O. Melikhova, Phys. Rev. B **65**, 094106 (2002)
14. J.I. Langford, in *Diffraction analysis of the microstructure of materials*, ed. by P. Scardi, E.J. Mittemeijer (Springer, Berlin, 2004)
15. T. Ungár, E. Schafler, J. Gubicza, in *Bulk Nanostructured Materials*, ed. by M.J. Zehetbauer, Y.T. Zhu (Wiley-VCH, Weinheim, 2009)
16. J. Gubicza, T. Ungár, Z. Kristall. **222**, 567 (2007)
17. G. Csiszár, Mater. Sci. Eng. A **609**, 185 (2014)
18. J. Gubicza, *X-ray line profile analysis in materials science* (IGI-Global, Hershey, 2014)
19. A. Leineweber, E.J. Mittemeijer, J. Appl. Cryst. **37**, 123 (2004)
20. P. Scardi, M. Leoni, Acta Mater. **53**, 5229 (2005)
21. L. Balogh, G. Ribárik, T. Ungár, J. Appl. Phys. **100**, 023512 (2006)
22. G. Csiszár, L. Balogh, A. Misra, X. Zhang, T. Ungár, J. Appl. Phys. **110**, 043502 (2011)
23. R. Kuzel, P. Klimanek, J. Appl. Cryst. **22**, 299 (1989)
24. P. Scardi, M. Leoni, Acta Cryst. A **58**, 190 (2002)
25. G. Ribárik, J. Gubicza, T. Ungár, Mater. Sci. Eng. A **387–389**, 343 (2004)
26. Z. Matěj, A. Kadlecová, M. Janeček, L. Matějová, M. Dopita, R. Kužel, Powder Diffr. **29**, S35 (2014)
27. J. Gubicza, A. Heczel, M. Kawasaki, J.-K. Han, Y. Zhao, Y. Xue, S. Huang, J.L. Lábár, J. Alloys Compd. **788**, 318 (2019)
28. C. Teena Mouni, S. Mahadevan, C. Ravishankar, K.A. Shaju, C.R. Das, P.K. Parida, A. Sagdeo, Mater. Sci. Eng. A **826**, 141960 (2021)
29. Y.H. Zhao, X.Z. Liao, Z. Jin, R.Z. Valiev, Y.T. Zhu, Acta Mater. **52**, 4589 (2004)
30. S.M. Yusuf, M. Hoegden, N. Gao, Int. J. Adv. Manuf. Technol. **106**, 4321 (2020)
31. G.K. Williamson, R.E. Smallman III., Philos. Mag. A **1**, 34 (1956)

32. G.K. Williamson, W.H. Hall, Acta Metall. **1**, 22 (1953)
33. J. Gubicza, L. Balogh, R.J. Hellmig, Y. Estrin, T. Ungár, Mater. Sci. Eng. A **400–401**, 334 (2005)
34. J. Gubicza, I. Schiller, N.Q. Chinh, J. Illy, Z. Horita, T.G. Langdon, Mater. Sci. Eng. A **460–461**, 77 (2007)
35. T. Kolonits, P. Jenei, B.G. Tóth, Z. Czigány, J. Gubicza, L. Péter, I. Bakonyi, J. Electrochem. Soc. **163**, D107 (2016)
36. J. Gubicza, M. El-Tahawy, Y. Huang, H. Choi, H. Choe, J.L. Lábár, T.G. Langdon, Mater. Sci. Eng. A **657**, 215 (2016)
37. G. Kapoor, Y. Huang, V. Subramanya Sarma, T.G. Langdon, J. Gubicza, Mater. Sci. Eng. A **688**, 92 (2017)
38. T. Kvackaj, A. Kovacova, R. Kocisko, J. Bidulska, L. Lityńska-Dobrzyńska, P. Jenei, J. Gubicza, Mater. Charact. **134**, 246 (2017)
39. Z. Bézi, G. Krállics, M. El-Tahawy, P. Pekker, J. Gubicza, Mater. Sci. Eng. A **688**, 210 (2017)
40. A. Heczel, F. Akbaripanah, M.A. Salavati, R. Mahmudi, Á. Vida, J. Gubicza, J. Alloys Compd. **763**, 629 (2018)
41. J. Gubicza, J.L. Lábár, J. Lendvai, N.Q. Chinh, J. Mater. Sci. **54**, 10918 (2019)
42. J. Gubicza, M. El-Tahawy, J.L. Lábár, E.V. Bobruk, M.Y. Murashkin, R.Z. Valiev, J. Mater. Sci. **55**, 16791 (2020) **(NQ Chinh)**
43. T. Krajnák, M. Janecek, P. Minárik, J. Gubicza, P.T. Hung, F. Novy, A.G. Raab, G.I. Raab, R. Asfandiyarov, Metals **11**, 63 (2021)
44. T. Krajnák, M. Janecek, P. Minárik, J. Vesely, P. Cejpek, J. Gubicza, P.T. Hung, D. Preisler, F. Novy, A.G. Raab, G.I. Raab, R. Asfandiyarov, Metall. Mater. Trans. A **52**, 1665 (2021)
45. L. Péter, É. Fekete, G. Kapoor, J. Gubicza, Electrochim. Acta **382**, 138352 (2021)
46. A.A. Khaleghi, F. Akbaripanah, M. Sabbaghian, K. Máthis, P. Minárik, J. Veselý, M. El-Tahawy, J. Gubicza, Mater. Sci. Eng. A **799**, 140158 (2021)
47. F. Akbaripanah, M. Sabbaghian, N. Fakhar, P. Minárik, J. Veselý, P.T. Hung, G. Kapoor, O. Renk, K. Máthis, J. Gubicza, J. Eckert, Mater. Sci. Eng. A **826**, 141916 (2021)
48. J. Gubicza, N.Q. Chinh, Z. Horita, T.G. Langdon, Mater. Sci. Eng. A **387–389**, 55 (2004)
49. K. Mathis, T. Krajnak, R. Kuzel, J. Gubicza, J. Alloys Compd. **509**, 3522 (2011)
50. Z. Hegedűs, J. Gubicza, M. Kawasaki, N.Q. Chinh, Zs. Fogarassy, T.G. Langdon, J. Alloys Compd. **536S**, S190 (2012)
51. J. Cízek, M. Janecek, T. Krajnak, J. Straska, P. Hruska, J. Gubicza, H.S. Kim, Acta Mater. **105**, 258 (2016)
52. J. Gubicza, S.V. Dobatkin, E. Khosravi, A.A. Kuznetsov, J.L. Lábár, Mater. Sci. Eng. A **528**, 1828 (2011)
53. J. Gubicza, N.Q. Chinh, J.L. Lábár, Z. Hegedűs, T.G. Langdon, Mater. Sci. Eng. A **527**, 752 (2010)
54. A. Heczel, M. Kawasaki, J.L. Lábár, J.-il Jang, T.G. Langdon, J. Gubicza, J. Alloys Compd. **711**, 143 (2017)
55. G. Kapoor, L. Péter, É. Fekete, J.L. Lábár, J. Gubicza, Mater. Charact. **145**, 563 (2018)
56. J. Gubicza, S. Nauyoks, L. Balogh, J. Labar, T.W. Zerda, T. Ungar, J. Mater. Res. **22**, 1314 (2007)
57. I. Kovács, L. Zsoldos, *Dislocations and Plastic Deformation* (Pergamon Press, London, 1973)
58. E. Schafler, G. Steiner, E. Korznikova, M. Kerber, M.J. Zehetbauer, Mater. Sci. Eng. A **410–411**, 169 (2005)
59. J. Gubicza, S.V. Dobatkin, E. Khosravi, Mater. Sci. Eng. A **527**, 6102 (2010)
60. R. Kuzel, M. Janecek, Z. Matej, J. Cizek, M. Dopita, O. Srba, Metall. Mater. Trans. A **41**, 1174 (2010)
61. J. Cizek, M. Janecek, O. Srba, R. Kuzel, Z. Barnovska, I. Prochazka, S. Dobatkin, Acta Mater. **59**, 2322 (2011)
62. Z. Hegedűs, J. Gubicza, M. Kawasaki, N.Q. Chinh, K. Süvegh, Z. Fogarassy, T.G. Langdon, J. Mater. Sci. **48**, 1675 (2013)
63. B.M. Iskakov, K.B. Baigisova, G.G. Bondarenko, Russ. Metall. (Metally) **2015**, 400 (2015)
64. E. Schafler, Scripta Mater. **62**, 423 (2010)
65. J. Gubicza, N.Q. Chinh, P. Szommer, A. Vinogradov, T.G. Langdon, Scripta Mater. **56**, 947 (2007)
66. J.W. Yeh, S.K. Chen, S.J. Lin, J.Y. Gan, T.S. Chin, T.T. Shun, C.H. Tsau, S.Y. Chang, Adv. Eng. Mater. **6**, 299 (2004)
67. B. Cantor, I.T.H. Chang, P. Knight, A.J.B. Vincent, Mater. Sci. Eng. A **375–377**, 213 (2004)
68. D.V. Shangina, J. Gubicza, E. Dodony, N.R. Bochvar, P.B. Straumal, NYu. Tabachkova, S.V. Dobatkin, J. Mater. Sci. **49**, 6674 (2014)
69. J. Gubicza, P.T. Hung, M. Kawasaki, J.-K. Han, Y. Zhao, Y. Xue, J.L. Lábár, Mater. Charact. **154**, 304 (2019)
70. P. Nagy, N. Rohbeck, Z. Hegedűs, J. Michler, L. Pethö, J.L. Lábár, J. Gubicza, Materials **14**, 3357 (2021)
71. T. Kolonits, Zs. Czigány, L. Péter, I. Bakonyi, J. Gubicza, Nanomaterials **10**, 2254 (2020)
72. T. Kolonits, P. Jenei, L. Péter, I. Bakonyi, Z. Czigány, J. Gubicza, Surf. Coat. Technol. **349**, 611 (2018)
73. T.J. Rupert, J.R. Trelewicz, C.A. Schuh, J. Mater. Res. **27**, 1285 (2012)
74. J. Hu, Y.N. Shi, X. Sauvage, G. Sha, K. Lu, Science **355**, 1292 (2017)
75. J. Gubicza, P.H.R. Pereira, G. Kapoor, Y. Huang, V. Subramanya Sarma, T.G. Langdon, Adv. Eng. Mater. **20**, 1800184 (2018)
76. T. Ungár, J. Gubicza, G. Ribárik, C. Pantea, T.W. Zerda, Carbon **40**, 929 (2002)
77. R. Vargas, D. Louer, J.I. Langford, J. Appl. Cryst. **16**, 512 (1983)
78. G. Csiszár, A. Misra, T. Ungár, Mater. Sci. Eng. A **528**, 6887 (2011)